

## Article

# Crystallization Kinetics of the $\text{Fe}_{68}\text{Nb}_6\text{B}_{23}\text{Mo}_3$ Glassy Ribbons Studied by Differential Scanning Calorimetry

Yongqin Liu <sup>1,\*</sup>, Man Zhu <sup>1</sup>, Yuanyuan Du <sup>2</sup>, Lijuan Yao <sup>1</sup> and Zengyun Jian <sup>1</sup>

<sup>1</sup> School of Materials and Chemical Engineering, Xi'an Technological University, Xi'an 710021, China; zhuman@xatu.edu.cn (M.Z.); yaolijuan@xatu.edu.cn (L.Y.); jianzengyun@xatu.edu.cn (Z.J.)

<sup>2</sup> Key Laboratory of Particle Astrophysics, Institute of High Energy Physics, Chinese Academy of Sciences, Beijing 100049, China; duyuan@ihep.ac.cn

\* Correspondence: liuyongqin@xatu.edu.cn; Tel.: +86-29-86173324

**Abstract:** Fe-based metallic glass has wide industrial application due to its unique mechanical behavior and magnetic properties. In the present work, the non-isothermal crystallization kinetics in  $\text{Fe}_{68}\text{Nb}_6\text{B}_{23}\text{Mo}_3$  glassy alloys were investigated by differential scanning calorimeter (DSC). The results indicate that both the glass transformation and crystallization process display an obvious kinetic effect. The activation energy is calculated using Kissinger's method and Ozawa's method. The activation energy for  $T_g$  (glass transition temperatures),  $T_x$  (crystallization initiation temperatures) and  $T_p$  (crystallization peak temperatures) calculated from Kissinger equation, is  $308 \pm 4$ ,  $342 \pm 5$  and  $310 \pm 7$  kJ mol<sup>-1</sup>, respectively. The activation energy for  $T_g$ ,  $T_x$  and  $T_p$  calculated from Ozawa equation is  $322 \pm 3$ ,  $356 \pm 5$  and  $325 \pm 7$  kJ mol<sup>-1</sup>, respectively. With the increase of the crystallization volume fraction  $x$ , the Avrami exponent  $n(x)$  first decreases and then increases. At the preliminary step,  $0 < x < 0.25$ ,  $2.5 < n(x) < 4.0$  stands for the growth from a small size with an increasing nucleation rate. When  $0.25 < x < 0.71$ ,  $n(x)$  decreases from 2.5 to 1.5, indicating that this stage is controlled by the growth of small particles with a decreasing nucleation rate.



**Citation:** Liu, Y.; Zhu, M.; Du, Y.; Yao, L.; Jian, Z. Crystallization Kinetics of the  $\text{Fe}_{68}\text{Nb}_6\text{B}_{23}\text{Mo}_3$  Glassy Ribbons Studied by Differential Scanning Calorimetry. *Crystals* **2022**, *12*, 852. <https://doi.org/10.3390/cryst12060852>

Academic Editor: Borislav Angelov

Received: 30 May 2022

Accepted: 15 June 2022

Published: 17 June 2022

**Publisher's Note:** MDPI stays neutral with regard to jurisdictional claims in published maps and institutional affiliations.



**Copyright:** © 2022 by the authors. Licensee MDPI, Basel, Switzerland. This article is an open access article distributed under the terms and conditions of the Creative Commons Attribution (CC BY) license (<https://creativecommons.org/licenses/by/4.0/>).

**Keywords:** metallic glasses; crystallization kinetic; activation energy; nucleation

## 1. Introduction

Fe-based amorphous glass has been widely used in the industrial field because of its excellent mechanical strength, outstanding magnetic properties and inexpensive material cost [1–6]. Thermodynamically, these metallic glasses are metastable materials. When heated to above the crystallization temperature, they transition into a crystalline phase. In order to precisely control the formation of the microstructure to fabricate new amorphous/nanocrystalline materials, it is of key importance to comprehend the nucleation as well as grain growth behavior in metallic glass. Differential scanning calorimetry (DSC) has been proven to be an effective way to study the crystallization kinetics of metallic glass. Traditionally, studies of the crystallization kinetics were performed on DSC equipment under non-isothermal crystallization and isothermal crystallization conditions. In previous studies, the effective activation energy, crystallized volume fraction, and transition kinetics have been analysed in detail [7–15]. Wang et al. [7] investigated the crystallization kinetics in the  $\text{Fe}_{80}\text{P}_{13}\text{C}_7$  alloys and proposed that the crystalline mechanism belongs to the diffusion-controlled growth of the glassy ribbons. Stoica et al. [8] studied the crystallization kinetics of the  $\text{Fe}_{66}\text{Nb}_4\text{B}_{30}$  bulk metallic glasses using the Johnson-Mehl-Avrami (JMA) and Kissinger equations. Studies on the  $\text{Zr}_{60}\text{Cu}_{20}\text{Al}_{10}\text{Ni}_{10}$  bulk metallic glass demonstrated that the crystalline mechanism is controlled by the JMA-like mode in the initial stage and later controlled by the normal-grain-growth (NGG) mode [9]. Lu et al. [10] studied the complex primary crystallization kinetics of the amorphous Finemet alloys and pointed out that the crystalline mechanism has one-dimensional growth at a near-zero nucleation rate for the crystalline volume fraction between 0.2 and 0.9. Although studies on the

crystallization kinetics have been carried out for a series of metallic glasses [7–15], data are still in deficiency on the crystallization kinetics of Fe-based metallic glasses.

It is important to understand the nucleation and grain growth behavior in metallic glasses in order to accurately control the formation of microstructure to fabricate novel amorphous/nanocrystalline materials. In this article, the crystallization kinetics of  $\text{Fe}_{68}\text{Nb}_6\text{B}_{23}\text{Mo}_3$  glassy alloys under non-isothermal conditions were studied by DSC. The crystallization kinetic parameters, i.e., activation energy, local activation energy and local Avrami exponent, were calculated to understand behaviors of the nucleation and the growth during the entire crystallization process.

## 2. Experimental Procedure

Nominally composed of  $\text{Fe}_{68}\text{Nb}_6\text{B}_{23}\text{Mo}_3$  (at.%), the master alloy ingots were made by the arc-melted pure elements of Fe (99.8%), Nb (99.9%), B (99.99%) and Mo (99.8%) in the atmosphere of Ti-gettered argon. To guarantee the compositional uniformity, the alloy ingots were remelted six times. The amorphous strip was made by injecting the molten alloy in a quartz tube into the rotating copper roller using the melt spinning method, with a linear velocity of  $40 \text{ m s}^{-1}$  and injection pressure of 20 kPa. The amorphous properties of the samples were tested with an X-ray diffractometer (D8 Advance, Bruker Company, Billerica, MA, USA), by using Cu  $K\alpha$  as a radiation. Thermoanalysis was implemented in DSC equipment (SDT Q600, TA Instruments, New Castle, DE, USA) in high purity argon and constant flow. A series of DSC scans at different heating rates were recorded over the heating rate range of  $10\text{--}40 \text{ K min}^{-1}$ .

## 3. Results and Discussion

### 3.1. Structure Analysis and Non-Isothermal Crystallization Behavior of the $\text{Fe}_{68}\text{Nb}_6\text{B}_{23}\text{Mo}_3$ Glassy Alloys

The XRD pattern of the melt-spun  $\text{Fe}_{68}\text{Nb}_6\text{B}_{23}\text{Mo}_3$  ribbons is shown in Figure 1. Its diffraction peak is wide, and there is no other peak corresponding to the crystal phase. The results show that the alloy can be completely amorphous under the present alloy composition.

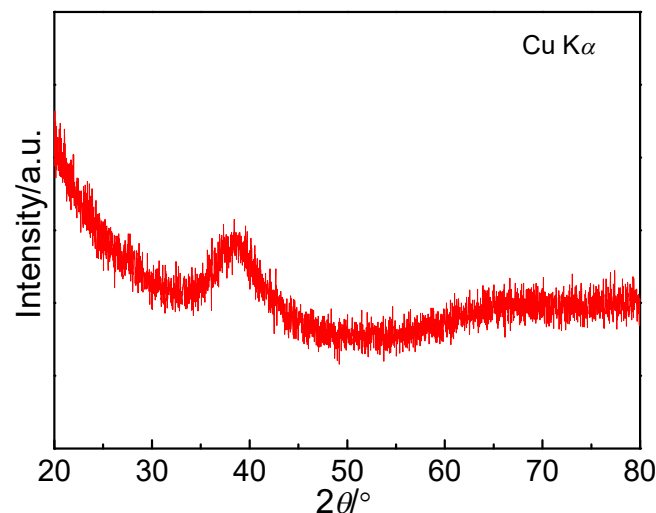
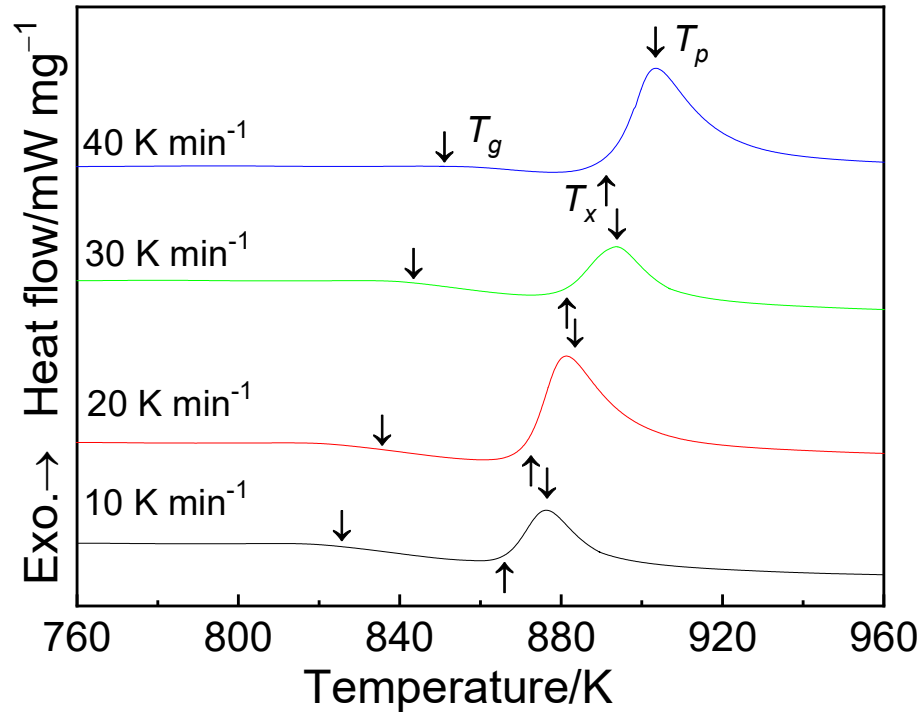


Figure 1. XRD pattern of the melt-spun  $\text{Fe}_{68}\text{Nb}_6\text{B}_{23}\text{Mo}_3$  ribbons.

Figure 2 shows the non-isothermal DSC traces of the  $\text{Fe}_{68}\text{Nb}_6\text{B}_{23}\text{Mo}_3$  amorphous band at different heating rates. All DSC traces show an endothermic process of the vitrification of the liquid to the undercooled state, followed by an exothermic reaction corresponding to the crystallization of the undercooled liquid. Table 1 lists the crystallization initiation temperatures ( $T_x$ ), glass transition temperatures ( $T_g$ ) and crystallization peak temperatures ( $T_p$ ), which are the characteristic temperatures. As the heating rate increases from 10 to  $40 \text{ K min}^{-1}$ , all the characteristic temperatures ( $T_x$ ,  $T_g$ ,  $T_p$ ) shifts to higher temperatures,

demonstrating that both the glass transition and the crystallization events have remarkable kinetic effects. As seen in Table 1, the supercooled liquid region  $\Delta T_x (= T_x - T_g)$  remains almost the same.



**Figure 2.** DSC traces for the  $\text{Fe}_{68}\text{Nb}_6\text{B}_{23}\text{Mo}_3$  glassy alloys under varied heating rates.

**Table 1.** Thermal properties of the  $\text{Fe}_{68}\text{Nb}_6\text{B}_{23}\text{Mo}_3$  glassy alloys under varied heating rates.

Heating Rate ( $\text{K min}^{-1}$ )	$T_g$ (K)	$T_x$ (K)	$T_p$ (K)	$\Delta T_x$ (K)
10	826	864	876	38
20	836	873	888	37
30	844	882	893	38
40	851	888	904	37

### 3.2. Activation Energy

The activation energy ( $E$ ) associated with the characteristic temperatures at different heating rates can be determined by Kissinger's Equation [16]:

$$\ln\left(\frac{T^2}{\beta}\right) = \frac{E}{RT} + \text{constant} \quad (1)$$

where  $\beta$  represents the heating rate,  $R$  denotes the gas constant and  $T$  represents  $T_x$ ,  $T_g$  or  $T_p$ . Using Equation (1) and the values of  $T_g$ ,  $T_x$  and  $T_p$  are listed in Table 1, the relationship plots between  $\ln(T^2/\beta)$  versus  $1/T$  can be drawn. Some approximately straight lines with a slope of  $E/R$  can be seen (Figure 3), from which the effective activation energy can be deduced. The effective activation energy of  $E_x$ ,  $E_g$ , and  $E_p$  are shown in Table 2.

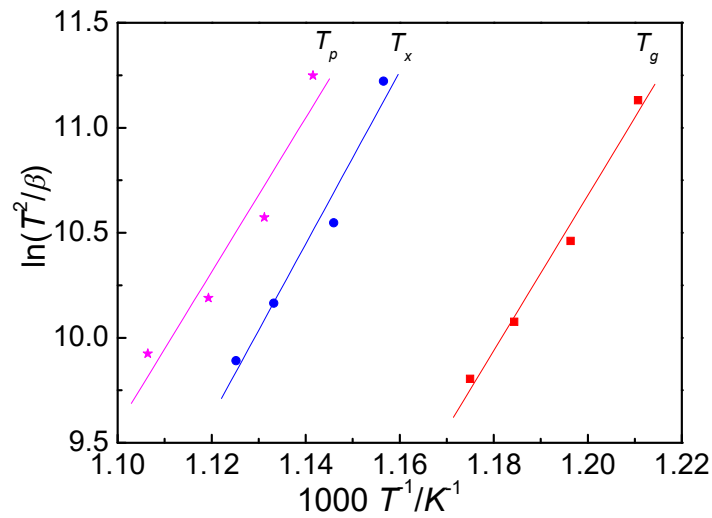


Figure 3. Kissinger plots of the  $\text{Fe}_{68}\text{Nb}_6\text{B}_{23}\text{Mo}_3$  glassy alloys.

Similarly, Ozawa plots, manifesting the relationship between  $1/T$  and  $\ln\beta$ , can also be obtained by using the Ozawa equation [17]:

$$\ln\beta = -\frac{E}{RT} + \text{constant} \quad (2)$$

Figure 4 reveals the relationship between  $1/T$  and  $\ln\beta$ . The activation energy can be deduced from the slope of  $-E/R$  using Equation (2). Table 2 also lists the activation energy of  $E_x$ ,  $E_g$  and  $E_p$  estimated from Ozawa equation. The effective activation energy of  $E_x$ ,  $E_g$  and  $E_p$  estimated from both the Kissinger and Ozawa equations have almost the same tendency. However, it can be seen that the values of effective activation energy deduced from the Ozawa equation are a bit higher than those deduced from the Kissinger equation. The crystallization kinetics of  $\text{Fe}_{67}\text{Nb}_5\text{B}_{28}$  alloy have been studied in the literature [15]. The values of  $E_g$ ,  $E_x$  and  $E_p$  calculated by Kissinger equation are equal to  $447 \pm 15$ ,  $536 \pm 22$  and  $559 \pm 20 \text{ kJ mol}^{-1}$ , respectively. The effective activation energies of  $E_g$ ,  $E_x$  and  $E_p$  calculated by the Ozawa equation are  $461 \pm 14$ ,  $551 \pm 24$  and  $574 \pm 20 \text{ kJ mol}^{-1}$ , respectively. The results determined from the two equations have the same tendency, while the activation energies estimated from the Kissinger equation are slightly smaller than those obtained from the Ozawa equation.

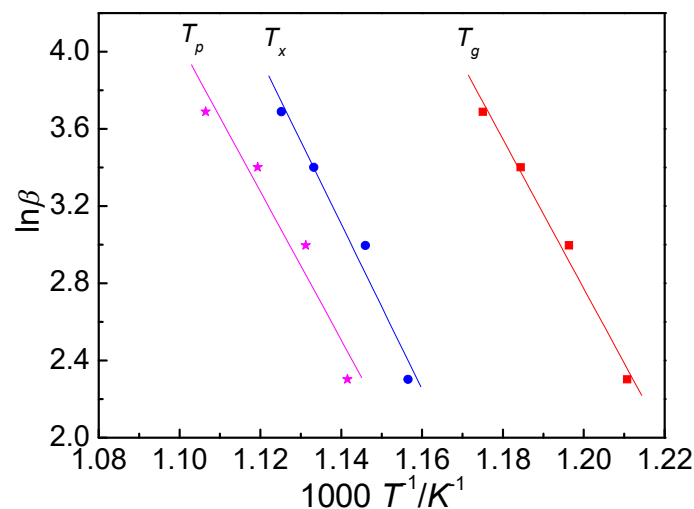


Figure 4. Ozawa plots of the  $\text{Fe}_{68}\text{Nb}_6\text{B}_{23}\text{Mo}_3$  glassy alloys.

It is already known that the crystallization initiation temperature is related to nucleation process and the crystallization peak temperature is directly associated with grain growth process.

**Table 2.** The calculated activation energy of the  $\text{Fe}_{68}\text{Nb}_6\text{B}_{23}\text{Mo}_3$  metallic glass.

Equation	Activation Energy ( $\text{kJ mol}^{-1}$ )		
	$E_g$	$E_x$	$E_p$
Kissinger	$308 \pm 4$	$342 \pm 5$	$310 \pm 7$
Ozawa	$322 \pm 3$	$356 \pm 5$	$325 \pm 7$

### 3.3. Local Activation Energy $E(x)$

The crystallization volume fraction  $x$  at a temperature  $T$  during the crystallization can be written as  $A_T/A_{\text{total}}$ , with  $A_T$  representing the corresponding area of the specific temperature  $T$ , while  $A_{\text{total}}$  represents the whole area of the crystallization peak in the DSC curve. According to the DSC traces, the relationship between the crystallization volume fraction  $x$  and temperature  $T$  of  $\text{Fe}_{68}\text{Nb}_6\text{B}_{23}\text{Mo}_3$  metallic glass for the crystallization event at different heating rates is shown in Figure 5. The slope of the  $x$ - $T$  curves denotes the crystallization rate at a stationary heating rate. The  $x$ - $T$  curves display a representative S-type shape. At the beginning and end of the  $x$ - $T$  curve, the crystallization rate is small, and when  $x$  is in the range of 10–80%, the crystallization rate is large. As the heating rate increases, the  $x$ - $T$  curve shifts to the right, revealing a typical thermal drive process.

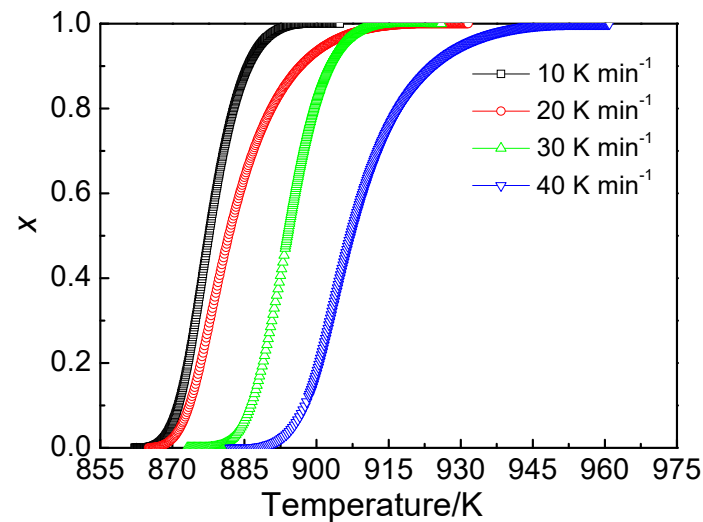


**Figure 5.** The  $x$ - $T$  curves of the  $\text{Fe}_{68}\text{Nb}_6\text{B}_{23}\text{Mo}_3$  glassy alloys under various heating rates.

According to the Ozawa-Flynn-Wall (OFW) equation, the local activation energy  $E(x)$  can be expressed as [18]:

$$\ln \beta = -1.0516 \frac{E(x)}{RT(x)} + \text{constant} \quad (3)$$

where  $E(x)$  and  $T(x)$  stand for the local activation energy and temperature corresponding to the given crystalline percent  $x$ , respectively.

Figure 6 shows that a curve of  $\ln \beta$  with respect to  $1000/T(x)$  at a specific value  $x$  can be derived from the fitting line.  $E(x)$  can be calculated from the slope of the fitting line when  $x$  is constant. Figure 7 exhibits the relationship between the variable activation energy of the  $\text{Fe}_{68}\text{Nb}_6\text{B}_{23}\text{Mo}_3$  metallic glass and the crystallization volume percent  $x$  during crystallization. It was found that the local activation energy decreases with the increase of the crystallization volume percent  $x$  during the crystallization.

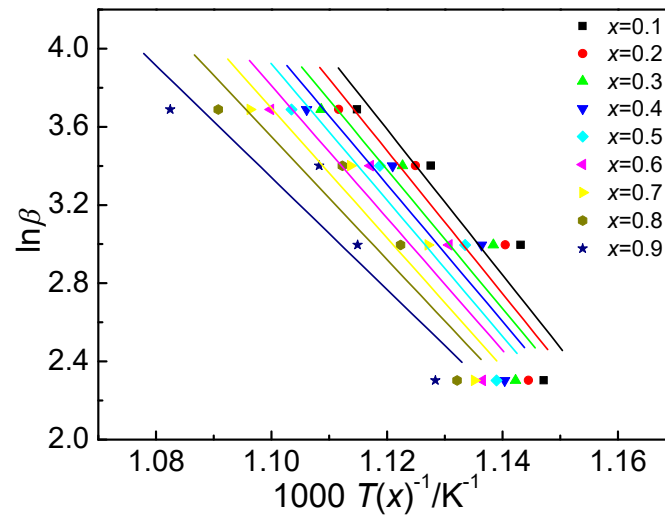


Figure 6. Plots of  $\ln\beta$  versus  $1000/T(x)$  of the  $Fe_{68}Nb_6B_{23}Mo_3$  glassy alloys.

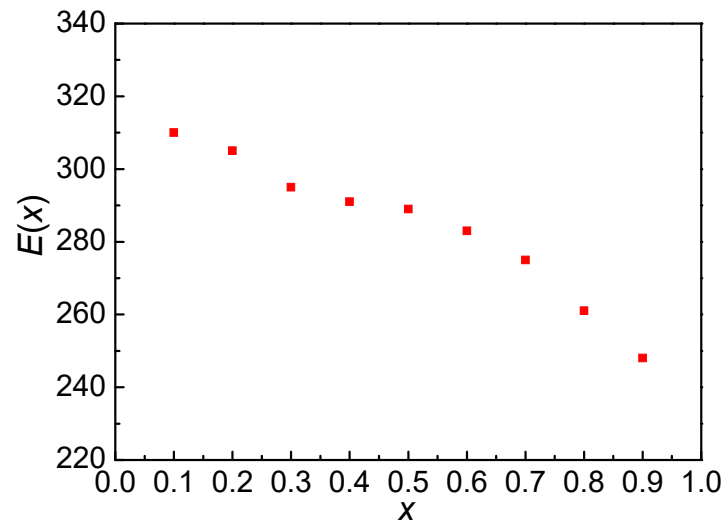


Figure 7. Relationship between local activation energy  $E(x)$  and the crystallization volume fraction  $x$ .

### 3.4. Local Avrami Exponent $n(x)$

During the phase transition, the local Avrami exponent ( $n(x)$ ) is important for understanding the mechanism of crystal nucleation and grain growth. The  $n(x)$  can be described as [10,19]:

$$n(x) = \frac{-R\partial \ln[-\ln(1-x)]}{E(x)\partial(1/T)} \quad (4)$$

Figure 8 displays the plots of  $\ln(-\ln(1-x))$  as a function of  $1000/T$  of the  $Fe_{68}Nb_6B_{23}Mo_3$  glassy alloys. The figure shows that there are many different stages during the crystallization process. The plots of  $n(x)$  versus  $x$  can be obtained by using Equation (4). Figure 9 exhibits the relationship between the local Avrami exponent  $n(x)$  and the crystallized volume percent  $x$  of the  $Fe_{68}Nb_6B_{23}Mo_3$  metallic glass with a heating rate of 20 K/min. During the whole crystallization process, the value of  $n(x)$  changes strongly with different  $x$ . The value of  $n(x)$  first decreases and then increases with the increase of  $x$ . At the initial crystallization stage ( $x < 0.05$ ), the value of  $n(x)$  is larger than 4.0. With the progress of crystallization,  $n(x)$  decreases slowly from 4.0 to 0.88, and  $x$  increases from 0.05 to 0.97. However, when the crystal volume percent further exceeds 0.97,  $n(x)$  is sharply increased to approximately 3.6.

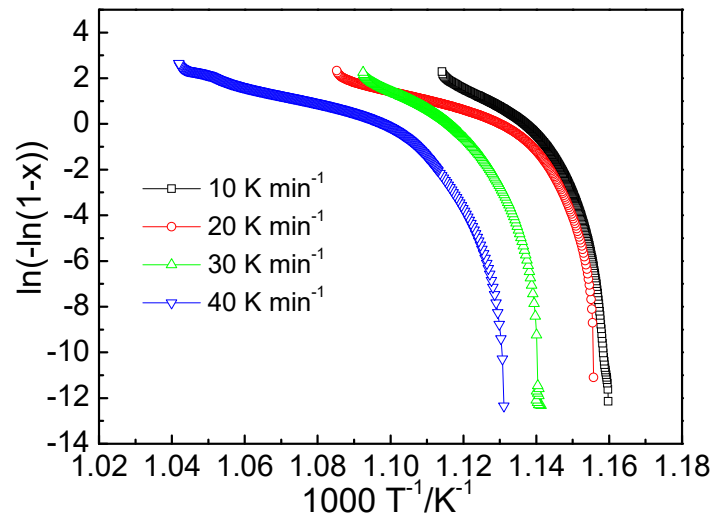


**Figure 8.** Plots of  $\ln(-\ln(1-x))$  against  $1000/T$  of the  $Fe_{68}Nb_6B_{23}Mo_3$  metallic glass (at 10\20\30\40 K/min).

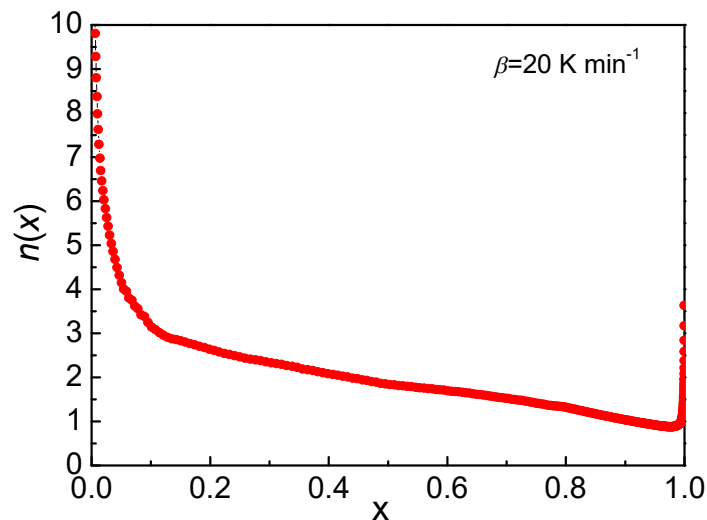


**Figure 9.** The variation of local Avrami exponent  $n(x)$  as a function of the crystallization volume fraction at heating rate of 20 K/min.

The Avrami exponent  $n(x)$  can be described as [20]:

$$n = a + b * c \quad (5)$$

where  $a$  is the nucleation index,  $b$  is the dimension of the growth,  $c$  is the growth index ( $c = 1$  and  $0.5$ , respectively, for interfacial control growth and diffusion control growth). The value of  $c$  is set at  $0.5$  for current metal because of the diffusion control growth in the Fe-based metallic glass [7].

The Avrami exponent  $n$  is an indicator of the nucleation and growth mechanism during the crystallization process. As the local Avrami exponent  $n(x)$  is bigger than 4 with no essentially meaning [20], it is not considered in the current study. In the initial stage of  $0 < x < 0.25$ , the value of  $n(x)$  ranges from 2.5 to 4.0, indicating that it grows from small dimensions with an increasing nucleation rate in the initial stage. The value of  $n(x) = 2.5$  stands for the growth from small dimensions with a constant nucleation rate. With the increase of  $x$  in the range  $0.25-0.71$ ,  $n(x)$  shows a decrease from 2.5 to 1.5, which represents the growth of small particles with a decreasing nucleation rate at this stage. The value of  $n(x) = 1.5$  stands for the grain growth at zero nucleation rate. The value of  $n(x)$

drops from 1.5 to 1.0, where  $x$  ranges from 0.71 to 0.97, illustrating that it is controlled by the particle growth with considerable original volume. In the final stage with  $x > 0.95$ , it was found that  $n(x)$  increases sharply to 3.6. The abnormal rise of  $n(x)$  at high  $x$  is attributed to the uneven distribution of nuclei in amorphous alloys [15,21].

### 3.5. Dependence of Glass Transition and Crystallization Event on Heating Rates

Figure 10 described the changes of  $T_g$ ,  $T_x$  and  $T_p$  with  $\ln\beta$  of the  $\text{Fe}_{68}\text{Nb}_6\text{B}_{23}\text{Mo}_3$  glassy alloys, which can be expressed by Lasocka's empirical relations [22]:

$$T = A + B \ln \beta \quad (6)$$

where  $A$  and  $B$  are constants, and  $\beta$  stands for the heating rate. The values of  $A$  and  $B$  are calculated by the least square method and are listed in Table 3. The value of  $B$  represents the response of the matrix to the configurational change in the glass transition region. With the increase of the  $B$  value, the characteristic temperature is more sensitive to the heating rate. The value of  $B$  for  $T_p$  is the largest, while the value of  $B$  for  $T_x$  is the smallest. Thus, the crystallization process is the most susceptible to the heating rate.

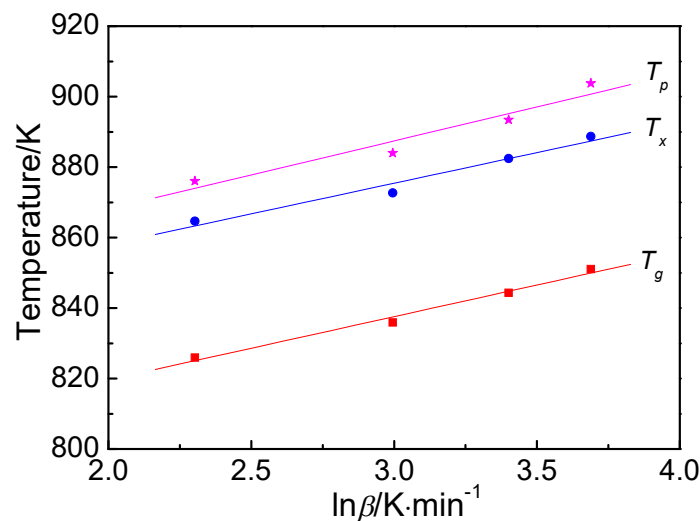


Figure 10. Relationship between  $\ln\beta$  and characteristic temperatures of the  $\text{Fe}_{68}\text{Nb}_6\text{B}_{23}\text{Mo}_3$  glassy alloys.

Table 3. Values of  $A$  and  $B$  of the  $\text{Fe}_{68}\text{Nb}_6\text{B}_{23}\text{Mo}_3$  glassy alloys.

	$T_g$	$T_x$	$T_p$
A	783.77	823.27	829.51
B	17.93	17.38	19.31

## 4. Conclusions

The purpose of the study of crystallization kinetics in this paper was to control the crystallization products and their size distribution, to obtain amorphous nanocrystalline alloys and to control their properties.

- Both the glass transition process and crystallization process display an obvious kinetic effect. The activation energy was calculated by using the Kissinger equation and the Ozawa equation. The values of  $E_g$ ,  $E_x$  and  $E_p$ , calculated by Kissinger equation, are  $308 \pm 4$ ,  $342 \pm 5$  and  $310 \pm 7$   $\text{kJ mol}^{-1}$ , respectively, and they are  $322 \pm 3$ ,  $356 \pm 5$  and  $325 \pm 7$   $\text{kJ mol}^{-1}$  calculated by the Ozawa equation, respectively.
- With the increase of crystallization volume fraction  $x$ , the Avrami exponent  $n(x)$  first decreases and then increases. The  $2.5 < n(x) < 4.0$  in the initial stage of  $0 < x < 0.25$  stands for the growth from small dimensions with an increasing nucleation rate. With

the increase of  $x$  in the range 0.25–0.71,  $n(x)$  decreases from 2.5 to 1.5, indicating that it is controlled by the growth of small particles with decreasing nucleation rate at this stage. The value of  $n(x)$  decreases from 1.5 to 1.0 with  $x$  ranging from 0.71 to 0.97, suggesting that it is controlled by the growth of particles with appreciable initial volume.

3. The fitting curves, using Lasocka's equation, clearly indicate that the course of the crystallization of  $\text{Fe}_{68}\text{Nb}_6\text{B}_{23}\text{Mo}_3$  is most susceptible to the heating rate.

**Author Contributions:** Conceptualization, Y.L. and M.Z.; methodology, Y.L., M.Z. and L.Y.; software, L.Y. and Y.L.; formal analysis, Y.L.; investigation, Y.L. and M.Z.; resources, Z.J.; data curation, Y.L. and Y.D.; writing—original draft preparation, Y.L., M.Z. and Y.D.; writing—review and editing, Y.L., M.Z. and Y.D.; supervision, Y.L., M.Z., L.Y., Y.D. and Z.J.; project administration, Y.L.; funding acquisition, M.Z. and Z.J. All authors have read and agreed to the published version of the manuscript.

**Funding:** This work was supported by the National Natural Science foundation of China (Grant No. 51301125) and the Natural Science Basic Research Program of Shaanxi Province (No. 2020JM-557).

**Institutional Review Board Statement:** Not applicable.

**Informed Consent Statement:** Not applicable.

**Data Availability Statement:** The data presented in this study are available on request from the corresponding author.

**Conflicts of Interest:** The authors declare no conflict of interest.

## References

1. Inoue, A.; Takeuchi, A. Recent development and application products of bulk glassy alloys. *Acta Mater.* **2011**, *59*, 2243–2267. [[CrossRef](#)]
2. Liu, T.; Lai, L.; Xiao, S.; Tang, M.; Zhang, H.; Guo, S. Ternary Fe–W–B bulk metallic glasses with ultrahigh thermal stabilities. *Mater. Sci. Eng. A* **2021**, *826*, 142034. [[CrossRef](#)]
3. Li, M.; Guan, H.; Yang, S.; Ma, X.; Li, Q. Minor Cr alloyed Fe–Co–Ni–P–B high entropy bulk metallic glass with excellent mechanical properties. *Mater. Sci. Eng. A* **2021**, *805*, 140542. [[CrossRef](#)]
4. Li, H.X.; Lu, Z.C.; Wang, S.L.; Wu, Y.; Lu, Z.P. Fe-based bulk metallic glasses: Glass formation, fabrication, properties and applications. *Prog. Mater. Sci.* **2019**, *103*, 235–318. [[CrossRef](#)]
5. Shen, B.L.; Chang, C.T.; Inoue, A. Superhigh strength and good soft-magnetic properties of (Fe, Co)-B-Si-Nb bulk glassy alloys with high glass-forming ability. *Appl. Phys. Lett.* **2004**, *85*, 4911–4913. [[CrossRef](#)]
6. Stoica, M.; Hajlaoui, K.; Lemoulec, A.; Yavari, A.R. New ternary Fe-based bulk metallic glass with high boron content. *Philos. Mag. Lett.* **2006**, *86*, 267–275. [[CrossRef](#)]
7. Wang, Y.; Xu, K.; Li, Q. Comparative study of non-isothermal crystallization kinetics between  $\text{Fe}_{80}\text{P}_{13}\text{C}_7$  bulk metallic glass and melt-spun glassy ribbon. *J. Alloys Compd.* **2012**, *540*, 6–15. [[CrossRef](#)]
8. Stoica, M.; Kumar, S.; Roth, S.; Ram, S.; Eckert, J.; Vaughan, G.; Yavari, A.R. Crystallization kinetics and magnetic properties of  $\text{Fe}_{66}\text{Nb}_4\text{B}_{30}$  bulk metallic glass. *J. Alloys Compd.* **2009**, *483*, 632–637. [[CrossRef](#)]
9. Zhuang, Y.X.; Duan, T.F.; Shi, H.Y. Calorimetric study of non-isothermal crystallization kinetics of  $\text{Zr}_{60}\text{Cu}_{20}\text{Al}_{10}\text{Ni}_{10}$  bulk metallic glass. *J. Alloys Compd.* **2011**, *509*, 9019–9025. [[CrossRef](#)]
10. Lu, W.; Yan, B.; Huang, W.-H. Complex primary crystallization kinetics of amorphous Finemet alloy. *J. Non-Cryst. Solids* **2005**, *351*, 3320–3324. [[CrossRef](#)]
11. Chen, Q.; Liu, L.; Chan, K.C. Crystallization kinetics of the  $\text{Zr}_{55.9}\text{Cu}_{18.6}\text{Ta}_8\text{Al}_{7.5}\text{Ni}_{10}$  bulk metallic glass matrix composite under isothermal conditions. *J. Alloys Compd.* **2006**, *419*, 71–75. [[CrossRef](#)]
12. Hu, X.; Qiao, J.; Pelletier, J.M.; Yao, Y. Evaluation of thermal stability and isochronal crystallization kinetics in the  $\text{Ti}_{40}\text{Zr}_{25}\text{Ni}_8\text{Cu}_9\text{Be}_{18}$  bulk metallic glass. *J. Non-Cryst. Solids* **2016**, *432*, 254–264. [[CrossRef](#)]
13. Prajapati, S.R.; Kasyap, S.; Patel, A.T.; Pratap, A. Non-isothermal crystallization kinetics of  $\text{Zr}_{52}\text{Cu}_{18}\text{Ni}_{14}\text{Al}_{10}\text{Ti}_6$  metallic glass. *J. Therm. Anal. Calorim.* **2016**, *124*, 21–33. [[CrossRef](#)]
14. Gong, P.; Zhao, S.F.; Wang, X.; Yao, K.F. Non-isothermal crystallization kinetics and glass-forming ability of  $\text{Ti}_{41}\text{Zr}_{25}\text{Be}_{28}\text{Fe}_6$  bulk metallic glass investigated by differential scanning calorimetry. *Appl. Phys. A* **2015**, *120*, 145–153. [[CrossRef](#)]
15. Zhu, M.; Fa, Y.; Jian, Z.; Yao, L.; Jin, C.; Nan, R.; Chang, F. Non-isothermal crystallization kinetics and soft magnetic properties of the  $\text{Fe}_{67}\text{Nb}_5\text{B}_{28}$  metallic glasses. *J. Therm. Anal. Calorim.* **2018**, *132*, 173–180. [[CrossRef](#)]
16. Kissinger, H.E. Reaction Kinetics in Differential Thermal Analysis. *Anal. Chem.* **1957**, *29*, 1702–1706. [[CrossRef](#)]
17. Ozawa, T. Kinetic analysis of derivative curves in thermal analysis. *J. Therm. Anal.* **1970**, *2*, 301–324. [[CrossRef](#)]

18. Flynn, J.H.; Wall, L.A. A quick, direct method for the determination of activation energy from thermogravimetric data. *J. Polym. Sci.* **1966**, *4*, 323–328. [[CrossRef](#)]
19. Zhu, M.; Li, J.J.; Yao, L.J.; Jian, Z.Y.; Chang, F.E.; Yang, G.C. Non-isothermal crystallization kinetics and fragility of  $(\text{Cu}_{46}\text{Zr}_{47}\text{Al}_7)_{97}\text{Ti}_3$  bulk metallic glass investigated by differential scanning calorimetry. *Thermochim. Acta* **2013**, *565*, 132–136. [[CrossRef](#)]
20. Christian, J.W. *The Theory of Transformations in Metals and Alloys*; Elsevier Science Ltd.: Oxford, UK, 2002; p. 546.
21. Sun, N.X.; Liu, X.D.; Lu, K. An explanation to the anomalous avrami exponent. *Scr. Mater.* **1996**, *34*, 1201–1207. [[CrossRef](#)]
22. Lasocka, M. The effect of scanning rate on glass transition temperature of splat-cooled  $\text{Te}_{85}\text{Ge}_{15}$ . *Mater. Sci. Eng.* **1975**, *23*, 173–177. [[CrossRef](#)]